THE ASTROPHYSICAL JOURNAL, 407:33–45, 1993 April 10

THE DARK MATTER DISTRIBUTION IN MS 2137−23 FROM THE MODELING OF THE MULTIPLE ARC SYSTEMS

YANNICK MELLIER, BERNARD FORT, AND JEAN-PAUL KNEIB
Observatoire Midi-Pyrénées, 14, Avenue Edouard Belin, 31400 Toulouse, France
Received 1992 May 5; accepted 1992 October 12

ABSTRACT

We model the cluster lens MS 2137−23 in which Fort et al. (1992) found a tangential arc, a radial arc, and some arclets. We show that by only using observational constraints given by the CCD images we can model the two arcs and predict the positions of the three arclets. These successful results give strong confidence on the structural and dynamical parameters of the cluster found. In particular, the core radius of the cluster is small, probably 3 times smaller than the value generally adopted. The amount of dark matter is large with a mass-to-light ratio of about 100 and a line-of-sight velocity dispersion of 1000 km s^{-1}. MS 2137−23 is the first case of a cluster lens in which we have enough distorted multiple images to really infer the distribution of dark matter in these systems. Therefore its study should be a first priority in the near future. Moreover, since the model is based on the assumption that the elongated radial structure is a radial arc, it is now urgent to get its redshift.

Subject headings: galaxies: clustering — gravitational lensing

1. INTRODUCTION

Fort et al. (1992) announced in a recent paper the discovery of the first possible radial arc in the distant cluster of galaxies MS 2137−23. This cluster is one of the 10 clusters of the Toulouse-Barcelona arc survey (ESO Key-Program 015-001-45K) in which a giant tangential arc has been observed. Its similarity with other arcs for which a redshift was successfully measured give us some confidence that it is a distorted image of a background source gravitationally lensed by the cluster. However, the reported observations have not been done in good weather and seeing conditions, and no ultra-deep images were obtained either at the NTT or at the CFHT runs. Nevertheless, the giant arc, the radial arc candidate, and some arclets are clearly visible and allow us to attempt a first model of the lens configuration. Actually, the simultaneous detection of both a tangential arc and a radial arc provide an interesting geometrical configuration and good constraints for modeling, compared to other cluster lenses for which only one giant arc has been detected.

Previous models of cluster lenses such as A370 (Hammer 1987; Kovner 1988; Grossman & Narayan 1989; Hammer & Rigaud 1989; Mellier et al. 1989), or Cl 2244 (Kovner 1988; Hammer & Rigaud 1989; Petrosian, Bergmann, & Lynds 1989) suffer so much from scarcity of data about the lens configuration that many different models can explain the same arc. Although, the mass-to-light ratio in the central region of clusters with giant arcs give convergent results, the question of the total mass distribution inferred from arc modeling in clusters of galaxies is still a pending one. In fact, the dark matter concentration as compared to the visible matter, and the extention of the invisible mass at large distance are unknown. Kochaneck (1990), Miralda-Escudé (1991), and Kneib, Mellier, & Longaretti (1993) discussed the possibility of using the statistical distribution of arclets in rich clusters of galaxies to infer the cluster potential. This approach looks interesting, although the authors stressed that uncertainties due to the redshift, the ellipticity, and orientation distributions of the background sources could give strong limits on the efficiency of this technique. One limitation is that it is impossible to get constraints on the core radius from the arclets in the weak distortion regime, unless external constraints or theoretical assumptions on the dynamical stage of the clusters are added. But in some cases, new X-ray observations done with the *ROSAT* satellite in some rich cluster lenses should give new constraints on the shape of the cluster and its central concentration so that a self-consistent model of the dark matter distribution should be performed with a high confidence level on the results.

A third interesting approach consists in the study of peculiar cluster lenses in which multiple arcs and a few arclets are detected. The first case of multiple arcs was the cluster Cl 0024+1654, originally discovered by Koo (1987), and the second is MS 2137−23 discovered by Fort et al. (1992). The aim of this paper is to emphazise the scientific interest of multiple arc systems through the study of MS 2137−23. In particular, we attempt to infer the total mass distribution of the distant cluster of galaxies MS 2137−23 by using the tangential giant arc, the radial arc, and the few arclets already detected. We did not try to investigate all the possibilities for making a giant arc in this system, but we mostly concentrated on consistent models which use as many observational constraints as possible. We therefore ask the following questions: is there any lens-model which can reproduce simultaneously the tangential and the radial arcs? If so, is there any self-consistent model only based on visible data which does not require additional ad hoc parameters about the dark matter potential? In this respect Fort et al. suggested that the faint diffuse stellar component around the central cD could provide good constraints on the potential geometry of the cluster. Indeed, MS 2137−23 offers a remarkable opportunity to model a cluster of galaxies and then to address the question of the dark matter distribution in these systems.

The second section of this paper summarizes the observational constraints from the data of Fort et al. In the third section we analyze the data in order to fix the rough lens configurations which could work to explain the arcs in MS 2137−23. The model is given in § 4, and we give the uncertainties and discuss the tricky points of the model in § 5. We show its implication for the dark matter distribution in § 6.

The conclusion reviews the future observations needed to confirm the modeling of this exceptional case of lensing which should provide the first reliable insights on the dark matter distribution in rich clusters of galaxies.

2. SUMMARY OF OBSERVATIONS

MS 2137−23 is an X-ray emitting cluster at a redshift of 0.313 (Stocke et al. 1991). The CCD observations do not show it as an extremely rich cluster as compared with other cluster lenses such as A370 (Mellier et al. 1988), A2390 (Pelló et al. 1991), or Cl 0024+1654 (Dressler & Gunn 1982). Indeed, within the critical radius defined by the giant tangential arc, only a few faint galaxies are visible, except in the center where the overbright cD galaxy is located (see Figs. 1 and 2 [Pls. 3 and 4]). Since the optical barycenter is completely dominated by the cD we can consider at this stage that the cD center is the cluster center.

Fort et al. (1992) show that the cD galaxy is surrounded by a large envelope which extends 15″ away from the center with an ellipticity $1 - b/a = 0.2$ and an orientation of 29°.5 with respect to the north axis (counterclockwise positive). These values are rather well measured because of the poor contamination by other faint galaxies.

The giant tangential arc is 12″ long and seems embedded within a faint arc halo which is about 2″ wide. The main blue bright structure has a width close to the seeing disk or below 0″.8. The arc is located at 15″.5 from the center. Its shape is roughly circular, but at least two discontinuities break the regular shape and split the arc into three segments. Furthermore, the surface brightness is not constant: (see Fig. 3 [Pl. 5]) the segment A02 is quite faint and shows a strong intensity enhancement in the middle. Segment A01 is much brighter than A02 but does not exhibit substructure. Segment A03 is faint, probably fainter than A02, and clearly escapes from the rough circularity of the overall arc. In a sense, segment A03 looks like the extended feature observed in the east side of the giant arc in A370 (Soucail et al. 1987).

The radial arc is located at 5″ from the cD galaxy and is exactly aligned toward the center of the cD. It is linear and extends over 5″, without obvious microstructures. It seems slightly brighter than the giant arc on all its points, but the contamination by the red envelope of the cD makes difficult an estimation of its magnitude and its color.

Finally, Fort et al. report the detection of some arclet candidates around the cluster center by using the weighted difference between the B and R CCD frames. Their positions are given in Figure 2.

3. OBSERVATIONAL CONSTRAINTS

As a starting point, our approach is to discuss whether or not there are some lens configurations which can explain the observed arcs by using a mass distribution in accordance with the light distribution. If at the end no model works properly we will consider the possibility of relaxing our optical constraints, which in part means that we will include some ad hoc free parameters. In this context, the observations give immediate constraints, and it is possible to exclude some lens models which would be inconsistent with the data in the framework of the thin transparent lens theory.

3.1. *Single Circular Lens*

We can exclude that MS 2137−23 is a single circular potential with an off-axis background source. Circular lenses lead to a second arc on the opposite side of the cluster center (towards the southern direction). The CCD image does not show such a secondary arc, although it should be an amplified image almost as large as the first one. The problem of a "missing" secondary arc was already discussed in detail by Hammer (1987) for the A370 cluster. Hammer concluded that it probably vanishes due to the lensing effect of the second overbright galaxy which is exactly located on its expected position. In MS 2137−23, there is no galaxy on the opposite position of the tangential arc with respect to the cD which could destroy a secondary arc. Furthermore, most of the visible galaxies are faint and could not even disrupt the images predicted by a single circular lens model. Therefore, the circular models can be ruled out from optical data, unless we assume the counter arc vanishes due to clumps of invisible mass which are not associated with galaxies. But, this possibility will not be considered seriously in the following.

3.2. *Single nearly Elliptical Lens*

The assumption that the cluster potential is elliptical is rather logical since it is the simplest model producing a single arc without a secondary counter-arc. In that case, two types of configurations can be discussed which depend on the location of the internal caustic with respect to the external caustic. Narayan & Grossman (1988) have summarized the most interesting cases for arc formations in nearly elliptical lenses. They show various configurations when the internal caustic is within the external caustic, and when two diametrically opposite internal cusps cross the external caustic line (see Figs. 2 and 3 of Narayan & Grossman 1988). Once the redshifts of the lens and the source are fixed, the two configurations depend on the core radius and on the ellipticity of the projected potential. Cases (a) and (b) give arcs when the source is located either on cusps or on folds. But in any case, it is not possible to get a tangential arc and a radial arc located on the same side with respect to the center of the lens with only one source. Therefore, in the case of a single elliptical lens model, we have to consider that the tangential arc and the radial arc come from two different sources.

Although elliptical potentials are the simplest models to explain the observation in MS 2137−23, their use increases the number of parameters since the orientation and the ellipticity are unknown. In the case of MS 2137−23 there are not enough bright galaxies to infer securely an orientation from the galaxy distribution around the arcs and the cD. On a larger scale, some bright galaxies are visible northwards, which indicate a possible orientation in the south-north direction. But they are far from the cD and they probably do not contribute to the local isopotential near the cD. For a similar reason, we did not consider bimodal potential, as the one described by Kassiola, Kovner, & Blandford (1992a) to model A2390 (Pelló et al. 1991). Moreover, the very bright saturated star near the galaxy excess detected in the north prevent seeing the galaxies in its surrounding which biases the galaxy counts toward the eastern region of the cluster. It is then difficult to infer the orientation from this galaxy excess. For these reasons we chose a local ellipticity and orientation based on the diffuse light distribution in the neighborhood of the dominant cD galaxy. Again this is our starting prescription to follow as much as possible the data as observational constraint. The final result of the modeling will be very interesting if these assumptions are compatible with the two arcs observed because although a good correlation was observed between the orientation of the brightest

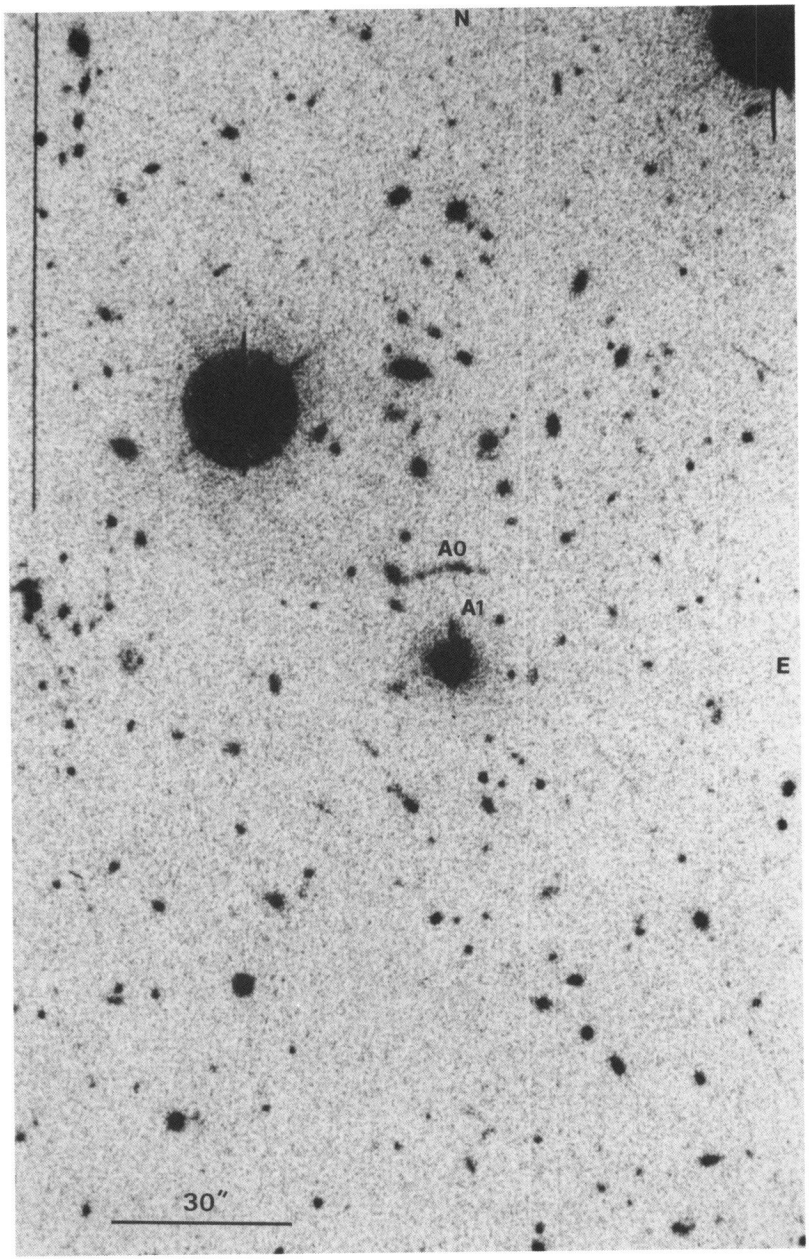

FIG. 1.—Large field *B* CCD frame of the cluster of galaxies MS 2137−23. The central bright object is the cD galaxy. The tangential arc on the north is clearly visible as well as the radial arc which appears to be much brighter than the giant arc. Most of the bright cluster galaxies are located toward the north and outside the critical line defined by the tangential arc.

MELLIER, FORT, & KNEIB (see 407, 34)

PLATE 4

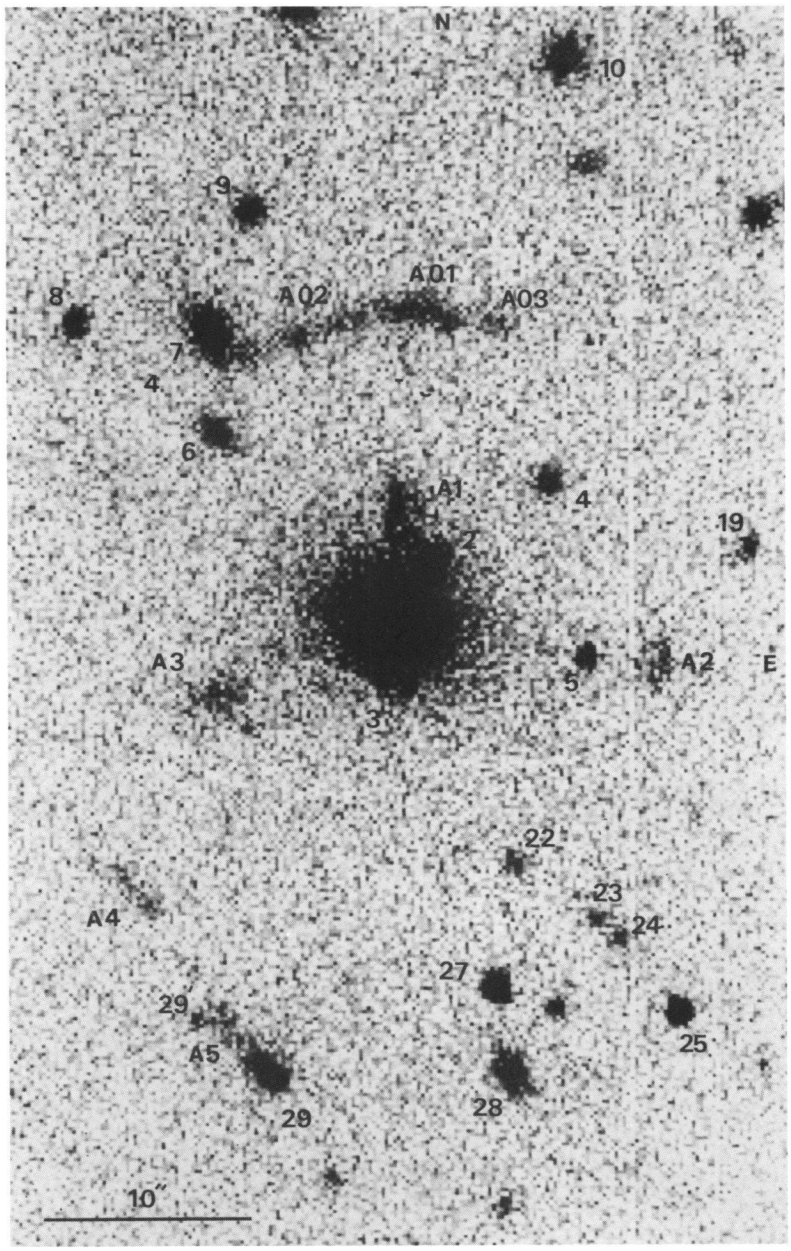

FIG. 2.—Zoom of the central region around the cD galaxy of MS 2137−23. Basically we do not see any galaxies within the critical line, except the cD. Galaxy 7 located on the western end of the tangential arc is rather bright and was included in the model as a perturbation. Note the position of the arclets found by Fort et al. (1992). The references of each object follow the one previously published by Fort et al.

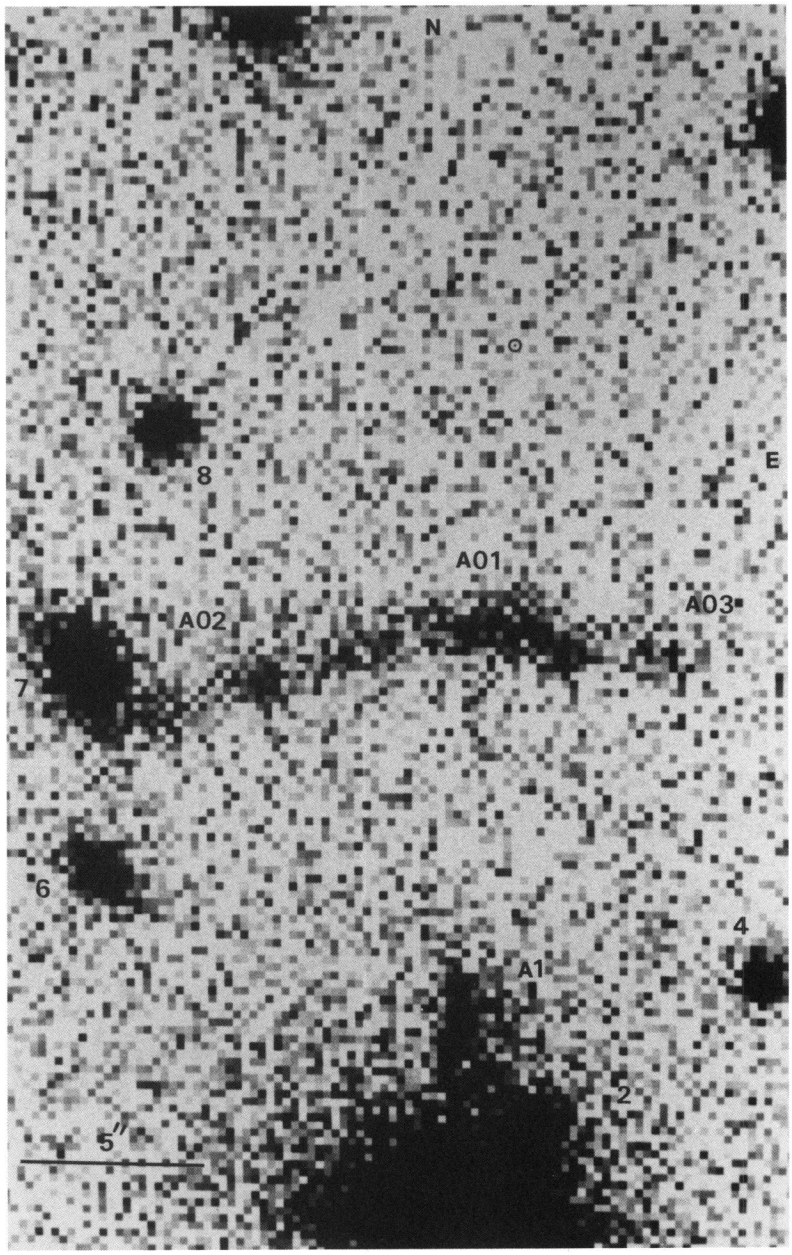

FIG. 3.—Zoom of the *B* CCD frame showing the structured component of the tangential arc. A01 is very bright as compared to the rest of the arc. A clear enhancement of intensity is visible on the center of A02. A03 is much fainter than the two other structures referenced in this paper. On the other hand, one cannot see any structure on the radial arc A1.

MELLIER, FORT, & KNEIB (see 407, 34)

cluster members and the overall galaxy distribution of X-ray maps (van Kampen & Rhee 1990; Porter, Schneider, & Hoessel 1991), the correlation between ellipticities remains unclear (Porter et al. 1991).

Since no other bright galaxies are visible around the overluminous cD galaxy, we will use the photometric data of Fort et al. (1992) and will assume that the cD envelope has isophotal contours which follow the projected mass density. The validity of the assumption will be justified further, according to the ability of such models to predict the positions of lensed galaxies in the image plane.

The use of geometrical parameters inferred from the photometric data of the cD for the projected potential of the cluster gives strong contraints on the modeling: if we assume that the isopotentials have a position angle equal to the isophotes of the cD (29°.5), it definitely rejects any model based on a source located on a cusp caustic since the cusp arcs are always located in the direction defined by the direction of the cusps. Therefore, in this context the tangential arc is necessarily a fold arc.

3.3. *Source Structures*

The images of the tangential arc show obvious structures on it. At least three regions with strong variations of the surface brightness are visible which definitely exclude that we are observing three images of the same source as in Cl 0024+1654 (Kassiola, Kovner, & Fort 1992*b*). Otherwise the three structures should have the same surface brightness. This is in favor of our initial assumption that we can exclude some peculiar case of strong or marginal lensing where the source is located on the cusp caustic and forms three images.

On the other hand, the structures observed on the arc are likely magnified structures of various regions of a single background galaxy. The interpretation of these structures are difficult, however, because of the poor spatial resolution of the CCD images. Furthermore, the fact that contamination by the bright galaxy near the eastern end of the arc is strong and that the signal-to-noise ratio on the ends of the arc is small preclude having good magnitudes and color indices all along the arc. We therefore consider the two following possibilities as equally probable: (a) we are observing a single image of a structured galaxy, such as a spiral system. The bright central region could correspond to the bulge, whereas the two elongated ends could be spiral arms. (b) The arc corresponds to a fold caustic configuration with two merging images of a same source with substructures. But since three regions are observable this implies that the two images correspond to different regions of a structured source, possibly a spiral system as in case (a).

The available observations of the radial arc do not show obvious structures or variations of its surface brightness. The contamination by the cD is strong and even an estimation of its magnitude is difficult. We will therefore consider this system as single source, either circular or elliptical but without a complex pattern which would add free parameters that are insufficiently constrained.

3.4. *Arclets*

At least four slightly elongated objects are visible on the CCD frames shown by Fort et al. which are classified as possible arclets on the basis of their color index. These small structures could be either weakly distorted individual background galaxies, multiple images of a single galaxy, or both. As with the giant arcs, it is extremely difficult to say whether they have the same surface brightness or colors as the arcs. It is interesting to notice that two of them (A2 and A4) have coordinates which are roughly compatible with what we could expect for secondary images of the giant tangential arc in the case of a background source located on a fold caustic. This particular system (tangential arc +A2 +A4) is an interesting constraint and we will look at it seriously in the next part.

3.5. *Source Redshift*

No spectroscopic redshifts of any arcs in MS2137−23 are available to date, although it should be a crucial point to confirm that the radial structure is actually a gravitational lensed image. However, we attempted to get some ideas of their redshift by comparing the $(B-R)$ and $(R-I)$ colors with a color redshift derived from the upgraded version of Bruzual's model (Charlot & Bruzual 1991).

The tangentially elongated arc could be at a redshift of 1.5 ± 0.5, but even with three-band photometry a large uncertainty remains on this value and it cannot be considered too seriously. This is worse for the radial arc because only two colors are available and its redshift is by no means constrained. For this reason we have assumed that the two sources are at the same redshift, considering models with source redshifts between the extrema $z = 0.5$ and $z = 3$ since below this critical value the lensing is expected to be inefficient, whereas for redshifts higher than 1 or so, the distance of the source becomes a negligible parameter. The consequence of this uncertainty of the source redshift is not dramatic for the image reconstruction, but it will imply an uncertainty on the velocity dispersion and the core radius of the lens itself and therefore on the total amount of dark matter.

4. THE LENS MODEL OF MS 2137−23

The lens is modelled by using a nearly elliptical projected potential, as it is commonly used by Blandford & Kochanek (1987) or Kovner (1988). The analytical potential has the following shape:

$$\Phi = 4\pi \left(\frac{\sigma_{1D}}{c}\right)^2 \frac{D_{LS}}{D_{OS}} \sqrt{r_c^2 + (1-\epsilon_\Phi)x^2 + (1+\epsilon_\Phi)y^2}\,, \qquad (1)$$

where $\epsilon_\Phi \simeq 1 - b/a$ (see Appendix A), r_c is a characteristic scale for the dense region of the cluster, which basically corresponds to the core radius, and finally σ_{1D} defines the efficiency of the lens for a given redshift of the source and the lens. It basically corresponds to the velocity dispersion of the lens, although it reduces to the line-of-sight velocity dispersion only in the case of a singular isothermal sphere (see Appendix B). This potential has the advantage of simplicity and allows analytical computations, but it is only valid for small ellipticity and for an ellipticity constant with radius.

The use of the extended envelope of the cD as an observational constraint for the model means that we assume that the projected luminosity is related to the projected mass density, even at large distance from the cluster center. If the projected potential is nearly elliptical with a small ellipticity ϵ_Φ, an orientation θ_Φ, and a two-dimensional typical radius r_c, the projected density is also nearly elliptical, with the same orientation, but an ellipticity $3\epsilon_\Phi$ and a core radius of about r_c (see Appendix A). Therefore, the projected density immediately gives constraints on the projected potential; that is $\theta_\Phi = 29°.5 \pm 4°$, $\epsilon_\Phi = 0.2/3 \pm 0.04$, and $r_c = 1''.5$. These values are inferred from a fitting of elliptic isophotal contours close to the cD center and on its external diffuse component. The errors are the

largest at the two extrema and are probably overestimated. The small variation of ellipticities of isophotes found from the smallest to the largest contours justifies our assumption that the ellipticity and orientation are roughly independent of radius. The value of r_c is the one observed around the cD galaxy and it could be different for the cluster. In fact, the dark matter distribution is the unknown key information the model should give ultimately. Therefore, we just use the geometry of the extended halo as an additional constraint, preferring not to use the core radius of the cD as a constraint for the cluster itself.

The modeling of the cluster lens was done by using several steps: (1) we only model the tangential arc by assuming that its orientation and ellipticity have the same values as the cD. These parameters are let free to move within the errors given by the observations, whereas r_c and σ_{1D} have no limits. (2) Once the best model is obtained, we add the second galaxy G2 as a perturbation for the image of the tangential arc and fit its parameter such that its velocity dispersion and core radius do not split the arc into two separate parts. This perturbing galaxy is not crucial for the model but it gives us extra information on the total mass of the perturbing galaxy and a better model for the western end of the arc. (3) When this model is satisfactory, then a second source at the same redshift is added to check whether or not it is possible to model simultaneously the radial and tangential arcs. (4) The uncertainties on the parameters of the best model are computed.

The general fitting procedure is described in Appendix C. Basically, it consists in computing the parameters of each source corresponding to an observed lensed image. Since multiple images should give a single source and then should have the same parameters in the source plane, the fitting is done by minimizing their differences.

The small arcs and the giant arcs cannot constrain the modeling in the same way. In the approximation of the weak distortion regime, each image can be represented as ellipses and are given by five parameters x_i, y_i, a_i, b_i and θ_i ($i = 1, \ldots, N$), which are, respectively, the center position, the major and minor axes, and the orientation of the individual ellipse. The number of constraints is reduced because we do not know the position and the shape of the source. Consequently, by assuming that the source is also given by five parameters, if we detect N images of a single source, the number of constraints is $5(N - 1)$. This is less than in the case of highly resolved images as in the modelling of radio rings (Kochanek et al. 1989) because the poor sampling of our image precludes use of each pixel as an individual constraint. But it is better than optical images of pointlike quasars, because the shape of two individual images is observable (A2 and A4).

On the other hand, the tangential arc and the radial arc are strongly magnified merging images, and most of their shape parameters are unknown, even for the center position which could have merged already. These pieces of information are actually very severe constraints. In particular they immediately give rather accurately the core radius of the lens (see Appendix D). Moreover, since the major axis of the amplification matrix gives the orientation of the major axis of the images at the merging point, we have three constraints at the crossing point where the external critical line crosses the merging images.

4.1. *Modeling the Tangential Arc*

Figure 4*a* displays the best model of the lens we found for the tangential arc with only one single potential for the cluster. The effect of the bright perturbing galaxy is shown on Figure 4*b*. The position of the sources is located where the fitting is the best with an elliptical source galaxy. That is, the positions of images, their thickness, and their length are the best ones. One can see that the western curvature is slightly increased and the arc is curved toward the cluster center. The overall shape of the arc is rather well fitted to the observational data. In particular, the arc gets thinner at the east and the central region of the source gives an image exactly located on the bump B1 which is clearly overluminous as compared to other regions of the arc. This could be easily explained by assuming that the core of the source is probably overbright.

The most amazing features are the positions of the two secondary images which are expected in case of a source on a fold caustic: both are located on the position of two detected arclets! One of them (A4) is perfectly located on the arclet with the same elongation and orientation. The second one (A2) is offset by 0.″5 but also has the right orientation and appears thicker than the first image, as it is observed. This remarkable coincidence shows that we are probably observing a fold arc with its associated multiple images of a single source. A pure coincidence is so improbable that this result is a strong argument in favor of the validity of our a priori assumption that the ellipticity and shape of the potential well are the same as the ones derived from the extended part of the cD. At this stage, it is important to notice that r_c and σ_{1D} are now constrained by the giant tangential arc and by the positions of the arclets A2 and A4 also. Therefore, since we are able to reproduce the three images at the right positions, the position of the source corresponding to a radial arc is unique.

4.2. *Modeling the Radial Arc*

Assuming the model is correct, we now search for the position of the source of the radial arc. This is rather easy since we only have to use the lens equation in a reverse way (that is from the image plane to the source plane) to infer the position of the observed radial arc in the source plane. Once the position is determined, all the images of the source are computed back to the image plan and we can check whether multiple images appear. The important point is that since we do not change anything in the lens model, if multiple images are predicted on the field where nothing is observed then the model could be rejected. This is a very severe test for the model.

Figures 4*c* and 5 give the final result: one can see that the second source reproduces the radial arc, as it is expected by positioning the source on the second caustic, and at the opposite side of the radial arc. But a second image is also predicted by the model which is located on a third observed arclet, with a right elongation and orientation!

4.3. *Final Result*

Table 1 summarizes the results of the model. The uncertainties given for the parameters are discussed in the next section. For comparison, we also give the main properties of the cD galaxies and the bright perturbing galaxy inferred from the photometric data. The observed line-of-sight velocity dispersion of the cD was estimated from the Faber-Jackson relation.

The amazing results are that the orientation and the ellipticity are similar to the cD values and that the core radius inferred from the model is very small, only 3 to 4 times the core radius of the cD galaxy. Furthermore, σ_{1D} is large and lies in

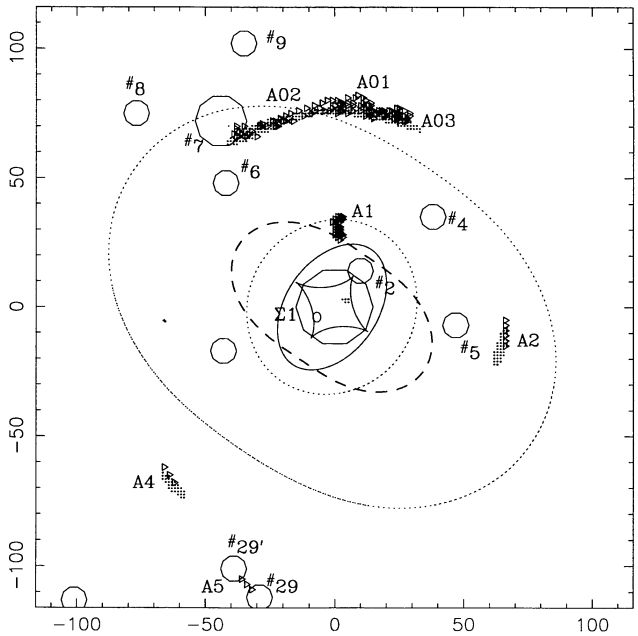

FIG. 4a

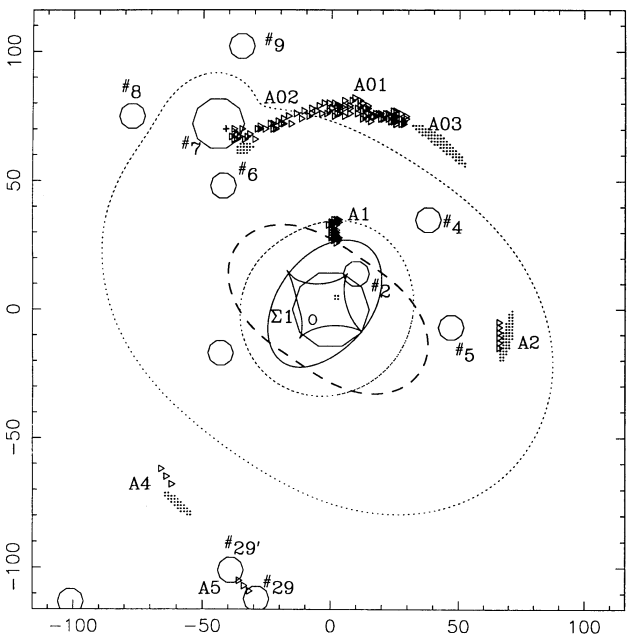

FIG. 4b

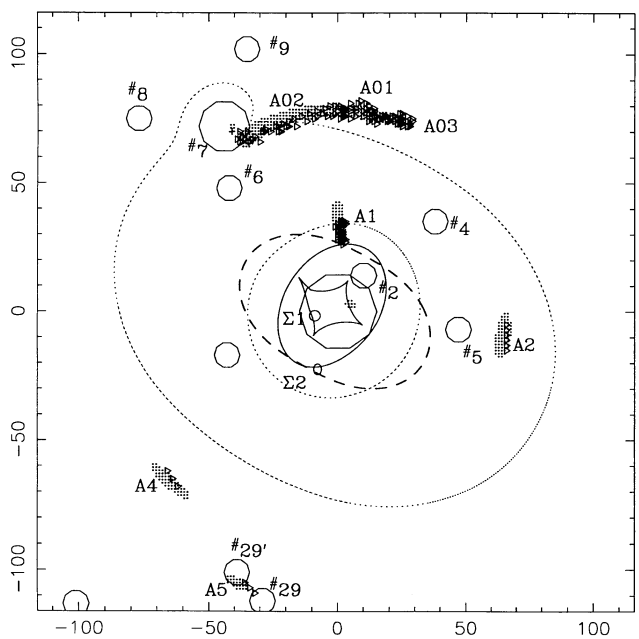

FIG. 4c

FIG. 4.—(*a*) Best model of the tangential arc with a single elliptical central potential. The polygons give the positions of some galaxies and the triangles show the arcs and arclets, as they are referenced on the CCD images of Fort et al. (1992). The dashed line gives the shape and the orientation of the projected potential. The dotted lines are critical lines and the full lines the caustics (*ellipse and diamond*). The source Σ1 is the ellipse near the cluster center. Note the position of the secondary images located on the arclets A2 and A4. The tangential arc given by the model is longer than the one observed, with a long extent near galaxy 7. (*b*) Same model as in Fig. 4*a*, but with a perturbation added to model galaxy 7. The maximum mass of the perturbation is limited by the tangential arc which must not be split into two segments on each side of this galaxy. However, the arc is broken and the eastern end is now too long. The modeling of A4 and A2 is also worse. The model could be improved by moving the source, as it is done on the next figure. (*c*) Best final model with the same potential as in Fig. 4*b* plus a second source (Σ2) for the radial arc. The radial arc is perfectly placed and the model predicts a second image of Σ2 between the two galaxies 29 and 29', very close to A5 with the same orientation. Note that on all the figures the elementary steps correspond to only 2″. The comparison with the image in Fig. 2 is really amazing.

TABLE 1

SUMMARY OF THE BEST MODEL FOR MS 2137−23 WITH TWO SOURCES

System	ϵ	θ	r_c	σ_{los} (km s^{-1})
Cluster model	$0.08^{+0.03}_{-0.03}$	$29°.5^{+9}_{-5}$	$8''^{+0.5}_{-2}$	1000
cD[a]	0.07 ± 0.04	$29°.5 \pm 5$	1.5 ± 1	350 ± 30[b]
Galaxy 7 model	0.04	8	0″.27	185
Galaxy 7[a]	0.07	8	...	230 ± 30[b]

NOTES.—The data given for the cD do not come from the model but from the observations of Fort et al. 1992, with the velocity dispersion inferred from the Faber-Jackson relation with the *B* CCD magnitudes scaled as in Grossman & Narayan 1988, 1989, but for $H_0 = 50$ km s^{-1} Mpc^{-1}. For galaxy 7, we give both the observational data and the result of the modeling.

[a] Observed.

[b] Deduced from the Faber-Jackson relation.

the range [1250–950] km s^{-1}, depending on the redshift assumed for the source ([0.5–3.0]).

5. UNCERTAINTIES AND PENDING PROBLEMS

5.1. *Uncertainties*

The uncertainties on the parameters we found for the best model are estimated with respect to the minimum χ^2 computed from equation (5) of Appendix D:

$$\chi^2 = \sum_{i=1}^{N} \frac{(w_{x_i} - w_{x_{i+1}})^2}{\sigma_{w_x}^2} + \sum_{i=1}^{N} \frac{(w_{y_i} - w_{y_{i+1}})^2}{\sigma_{w_y}^2} + \sum_{i=1}^{N} \frac{(\xi_{x_i} - \xi_{x_{i+1}})^2}{\sigma_{\xi_x}^2} + \sum_{i=1}^{N} \frac{(\xi_{y_i} - \xi_{y_{i+1}})^2}{\sigma_{\xi_y}^2}, \quad (2)$$

where the differences are computed in the source plane.

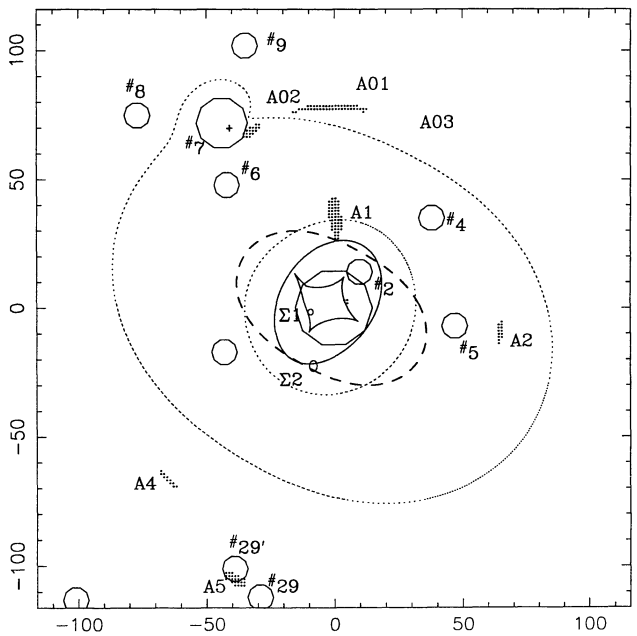

FIG. 5.—Position of the central region of the source from the model given in Fig. 4*c*. The elongated right-hand image is located on the overbright region A01 of the tangential arc, with roughly the same shape. The second image is not located on A02, with an offset of about 10″, which is quite large and unsatisfactory. Therefore, although the prediction is not so bad, the assumption that the bright regions of the arc come from a bright bulge of the source is not conclusive.

The dispersion σ_{w_i} comes from the undimensioned lens equation

$$w = \frac{r_c}{\Phi_0}(r - \nabla_{r\varphi}) . \tag{3}$$

By assuming that the small arcs are weakly distorted images, their center positions are known to within 1 pixel. The corresponding error in the source plane is reduced by a factor which should be close to the angular deviation R_T. Therefore, the error on the position in the source plane is

$$\sigma_{w_x} \simeq 2\frac{\sigma_x}{R_T} ,$$

where σ_x is the error of the center position along the x-axis in the image plane. Since $R_T \simeq 15''$ and $\sigma_x = 0''.2$ (1 pixel), the source center is always well positioned.

The shape parameter $\xi = 0.5(a/b - b/a)$ (see Appendix C) gives an error of about $\sigma_\xi \simeq \sigma_a/b$, where a and b are, respectively, the major and minor axis of the ellipses. In the weak distortion regime, the major axis is known to within one pixel, and b is about 10 pixels (see Fig. 2), and therefore $\sigma_\xi \simeq 0.2$.

The uncertainties are given by computing χ^2/ν, where ν is the total degree of freedom in the model, for a confidence level of 90%. The error on r_c is, however, much constrained by the radial arc which gives an upper limit of $r_{c\max} = 8''.5$. If r_c is larger than the maximum value, the image of the second source is not radial anymore. The following results summarize the best model:

$$0.05 < \epsilon_\Phi < 0.11 ,$$

$$24^\circ.5 < \theta_\Phi < 38^\circ.5 ,$$

$$6'' < r_c < 8''.5 \quad \text{or} \quad 35\, h_{50}^{-1} < r_c < 55\, h_{50}^{-1} .$$

5.2. *Problems*

Although the simplest model described above remarkably fits the observables, it is far from explaining all the data already available:

Arclet A2.—The positions of the observed arclet A2 and the image from the model differ by about 3 pixels (0″.6). At this stage of the modeling, the difference is not explained except if we assume that local variations of the ellipticity of the potential are present. It seems clear that if we want to go further in the accuracy of the modeling we can even question seriously the validity of the simple analytical formula we used to describe the projected potential.

Tangential arc and shape of the source.—The tangential arc shows some regions with strong variations of intensity and also some discontinuities with respect to a circular arc which cannot be explained with our single elliptical source model (see Fig. 5). Previous works done in some other giant arcs already suggested that most of the complex substructures observed come from intrinsic properties of the sources. In particular, spiral galaxies or interacting systems with double or triple galaxies have been suggested in A370 (Mellier et al. 1989), Cl 2244−02 (Hammer & Rigaud 1989) or in A2390 (Mellier et al. 1989; Kassiola et al. 1992a). In the case of MS 2137−23, the intensity enhancement observed on A01 could be the image of a central bright bulge, as observed in some late-type spiral of S0s. The model predicts that two increases of intensity should be observed on the arc, with one of them exactly at the position of A01 and a second one close to the bright region of A02, but not exactly on it. This suggests that we are probably observing a structured galaxy. However, at this stage, the description of most details observed in MS 2137−23 need much better data with high resolution imaging in several colors because we cannot constrain further the model from present day images. It is obvious that our source model is too naive.

Arclet A5.— The position predicted by the model is shifted by 3 pixels with respect to the observed image.

6. THE DISTRIBUTION OF DARK MATTER IN MS 2137−23

Generally, an estimate of the dark matter distribution in clusters of galaxies from arc models is rather questionable because we have many more free parameters than observational constraints. In the peculiar case of MS 2137−23, we give a model which fits two giant arcs with only two free parameters (the core radius and the velocity dispersion), and successfully predict the positions of three arclets. The efficiency of the modeling is due to the large number of multiple images we have, as in Cl 0024+1654, in which three arcs are visible (Kassiola et al. 1992b). However, even for Cl 0024+1654 there is no prediction on the position of new images, and from this point of view MS 2137−23 is unique and probably the best model ever done for cluster lenses.

Some very important remarks can be made:

1. Since we observe a radical arc located at 5″ from the cD center, it definitely establishes that cD clusters of galaxies cannot be represented as singular isothermal systems but have a finite core size, and this induces the possibility of having radially merging images located near the core radius (Blandford & Kochanek 1987). This also confirms that its value should be close to 5″.

2. The core radius of the projected potential inferred from the model is very small (8″, or 50 h_{50}^{-1} kpc). Even if the uncer-

tainty of the model was large, it is clear that the radial arc is between 5″ to 9″ and therefore the core radius is definitely small. This surprising result is in contradiction with what is still generally admitted from studies on clusters of galaxies based on the galaxy distribution or X-ray maps. However, it is in favor of the guesses of Hammer (1991) that the thinness of arcs already detected means that cluster mass density is highly peaked, and is in agreement with the small core radius found in A1689 by Tyson, Valdes, & Wenk (1990) from the arclet distribution around the cluster. It is also corroborated by the new X-ray investigations of cD clusters done by Eyles et al. (1991) in the Perseus Cluster, Gerbal et al. (1992) on the nearby clusters A85 and A2199, who found values of core radii exactly in the same range as this model, and Briel, Henry, & Böhringer (1992) from the *ROSAT* observations of the Coma cluster who concluded that the dark matter should be baryonic. A comparison of our model with the X-ray mass distribution is difficult, however, because the resolution of the Extended Medium Sensitivity Survey is only 2.′4 × 2.′4, which is much larger than the core radius and the critical radius (15″) we found, and is about the size of the overall CCD frame (Gioia et al. 1990).

3. Surprisingly, the shape parameters of the cluster (ellipticity, orientation) given by the best model are the same as the cD's parameters inferred from the photometry. This result confirms the previous works by van Kampen & Rhee (1990) and Porter et al. (1991) that cD galaxies are aligned with the cluster light and X-ray distribution. However, the correlation between the cluster ellipticity and the cD ellipticity is quite new. In particular, the ellipticity of the potential is constant, even at a large radius and it is not needed to have a smaller ellipticity above 30 kpc to perfectly match the image of the giant tangential arc. This disagrees with the flat optical shape of the cD with respect to its host cluster mentioned by Porter et al. But the comparison with their results is difficult since we did not include a variation of ellipticity with radius.

4. The total mass included within the external critical radius is within the range 3–7 × 10^{13} $M_\odot$ for a redshift between 3 to 0.5. This corresponds to a M/L_R between 170 to 70. Furthermore, the total mass within the internal critical radius and for the same redshift range of the source is between 20–9 × 10^{12} $M_\odot$ and corresponds to an M/L_R between 70 to 30 within the core radius of the cluster. The variation of the M/L_R by only a factor of 2 to 3 on the scale of the cD galaxy may be due to the different core radii of the cluster and the cD. But it could be due to our choice for the analytical shape of the projected potential or to small perturbations of the mass distribution of the dark matter with respect to the density mass we inferred from the model. A better estimate of the evolution of the mass-to-light ratio with radius would be required to separate the potential in two components, one for the luminous matter associated with the cD and the other for the dark matter. At this stage of the modeling we cannot separate the components because we have not enough constraints from our observations. High-resolution images of the central region are needed to go further. On the other hand, the light distribution is only based on the cD since this is the only galaxy visible within the external critical radius. Therefore the cluster light distribution is statistically meaningless on this scale, and this uncertainty could explain the variation with radius of the mass-to-light ratio. On scales larger than the external critical radius, the model itself is getting worse with the increasing radius, with possible changes of its structural parameters, and the evolution with radius of the M/L_R of our model are inconclusive.

5. The velocity dispersion (σ_{1D}) decreases from 1250 to 950 km s^{-1}, when the source redshifts increase from 0.5 to 3.0. However, in order to compare this value to the one computed in numerical simulations we must relate the σ_{1D} of the modeling to the σ_{los}. By using the analytical projected potential given in this paper, there is a small discrepancy between these two velocities which is expressed in Appendix B. In that case, the true velocity dispersion (that is, the square root of the variance) is the one computed in the model reduced by a factor of $\sqrt{3}/2$. Therefore, the line-of-sight velocity dispersion ranges from 800 to 1100 km s^{-1} for a redshift of the source ranging from 3.0 to 0.5. These values are compatible with the observed ones in most rich clusters of galaxies, but in any case this is high compared with the velocity dispersion expected from the standard CDM predictions (Frenk et al. 1990), where clusters with a velocity dispersion of about 1000 km s^{-1} are extremely rare. It is interesting to notice that the values given by the modeling are independent of the spectroscopic radial velocities and consequently, no bias or projection effect leading to spurious velocities can be suspected. Furthermore, the CCD images in *B* and *R* show that between the cD galaxy and the tangential arc there are only a few faint galaxies and we cannot suspect that MS 2137−23 is constituted of superposed clusters on the line of sight at different redshifts which could give a large amount of projected mass. The arguments suggested by Frenk et al. (1990) to explain the number of high-velocity dispersion clusters observed do not hold at all in the case of MS 2137−23. A similar conclusion is given by Smail et al. (1992) for the distant cluster AC 114 where the authors found a high-velocity dispersion and a mass distribution oriented in the same direction as the galaxy distribution. Actually, in most of the cluster lenses in which models have been done, the inferred velocity dispersion is much higher than the CDM prediction and confirms the line-of-sight velocity dispersions measured from spectrospic data, which are more than 1000 km s^{-1} in most cases (Mellier 1993). These are strong arguments that the occurence of clusters with high-velocity dispersion cannot be explained only by projection effects, and are much more numerous than the standard CDM predictions.

7. CONCLUSIONS

The observations of two different arc systems with multiple images (arclets) in the distant cluster of galaxies MS 2137−23 provide for the first time in the Toulouse-Barcelona arc survey an overconstrained model of an elliptical potential. We have shown that the central cD galaxy gives a direct measurement of the ellipticity and the orientation of the projected potential of the cluster. An important consequence is that the same approach should be attempted for other cD clusters with a single multiple arc system, such as A1942, or A2163, or even for clusters dominated by two cDs or giant ellipticals such as A370, although one has to check carefully that no twisted isophotes are present.

The amazingly successful predictions are strong arguments to believe in the final results about the dark matter distribution inferred from the model. In particular, the amount of dark matter with respect to luminous matter is large and its seems highly peaked, with a finite core radius more than 3 times smaller than standard values, and displays a distribution similar to the cD. The remarkable similarity between the ellipticity and orientation of the cD and the cluster is confusing. What is the physical meaning of this, in terms of the velocity dispersion of stars within the cD itself? Actually, since we have no information about the kinematics of the stellar component

in the cD we cannot separate the cluster dark matter component and the cD stellar distribution from our model, and therefore we cannot really infer dynamical properties of cluster cDs. It is clear that medium-resolution spectroscopy of the stellar component of the cD itself is now needed to separate the cluster and the cD potential wells.

Most of these results are based on the assumption that the extended straight structure near the cD galaxy is a radial arc. It is, then, urgent now to get its redshift to confirm its gravitational origin. The central distribution of the cluster itself will be definitely constrained when both redshifts of the radial arc and the tangential arc will be measured. These two measurements are then the first observational priority. On the other hand, we could have a much better model of the lens configuration once detailed structures observed in high-resolution imaging of the arcs is available. This is now the only way to go further in the knowledge of the sources.

The present paper shows the efficiency of imaging and photometry for modeling cluster lenses. They are actually more efficient than spectroscopic data because the positions and shapes of arcs and arclets do have much more information about the potential well than the redshifts of the elongated structures do. Most of our results concern the center of the lens. But the same analysis could be done far from the center by using ultra-deep CCD frames, at distances where the large number of faint weakly distorted sources compensate for the poor efficiency of the lens.

We thank A. Kassiola, C. Kochanek, I. Kovner, P.-Y. Longaretti, G. Mathez, J. Miralda-Escudé, and G. Soucail for useful discussions and encouragements during the redaction of this paper and also the referee for its number of useful comments. Many thanks to M. Cailloux for her assistance in data reduction and pictures preparation. The modeling was partly done with an upgraded version of the software kindly provided by I. Kovner. The photometric redshifts were estimated from the new version of Bruzual's models who implemented his code in Toulouse.

APPENDIX A

DEFINITIONS OF CORE RADII AND RELATION BETWEEN THE PROJECTED POTENTIAL AND THE PROJECTED DENSITY

The approximated projected potential used in this paper is

$$\Phi(x, y) = \Phi_0 \sqrt{1 + (1 - \epsilon)x^2 + (1 + \epsilon)y^2}\,, \tag{A1}$$

where $\epsilon = (a^2 - b^2)/(a^2 + b^2)$ is the ellipticity and x and y are scaled to the core radius ($x = x'/r_c$ $y = y'/r_c$).

The trace of the amplification matrix gives the pojected mass density:

$$\sigma(x, y) = \tfrac{1}{2}\nabla^2\Phi\,, \tag{A2}$$

which we write as follows in undimensioned coordinates:

$$\sigma(x, y) = \frac{1}{2}\frac{2 + x^2 + y^2}{[1 + (1 - \epsilon)x^2 + (1 + \epsilon)y^2]^{3/2}}\,, \tag{A3}$$

where the terms in ϵ^2 have been neglected.

We can compare this formula to the projected profile given by the modified Hubble law which follows the King family models up to typically four core radii:

$$\Sigma_K(x, y) = \frac{2}{1 + (r/r_c')^2}\,. \tag{A4}$$

In the case of spherically symmetric systems $\sigma(0) = 1$ and $\Sigma_K(0) = 2$, whereas $\sigma(r_c) = 0.53$ and $\Sigma_K(r_c') = 1$. That is, the scale factor used in our analytical projected potential is equivalent to the core radius of a King model. Since the observers usually fit the projected profile to a Hubble law, the typical scale of the observed profile is also roughly equivalent to the core radius of a King model. Therefore the core radius of the cD galaxy in MS 2137−23 is given for $I(r_c'') = I_0/2$, where I_0 is the central intensity.

The other point is the link between the ellipticity of the projected mass density and the projected potential. Assume that we observe a galaxy with isodensity contours σ_1 given by equation (A3). We have

$$2\sigma_1\,[1 + (1 - \epsilon)x^2 + (1 + \epsilon)y^2]^{3/2} = 2 + x^2 + y^2\,. \tag{A5}$$

Set

$$t = 1 + x^2 + y^2 \qquad \text{and} \qquad u = x^2 - y^2\,.$$

Then equation (A5) becomes

$$4\sigma_1^2[t^3 - 3t^2\epsilon u + 3t\epsilon^2 y^2 - \epsilon^3 u^3] = (1 + t)^2\,.$$

In the case of small ellipticities, we have

$$|3t^2\epsilon u| \gg |3t\epsilon^2 u^2|\,.$$

Therefore,

$$4\sigma_1^2[t^3 - 3t^2\epsilon u] = (1 + t)^2\,, \tag{A6}$$

that is,

$$t - 3\epsilon u = \frac{1}{4\sigma_1^2}\left(1 + \frac{1}{t}\right)^2 . \tag{A7}$$

Let us consider now the limiting cases where $x = y = 0$ and x and y are infinite. The factor $(1 + 1/t)^2$ of equation (A7) varies from 4 to 1 and then $t - 3\epsilon u$ varies from $1/\sigma_1^2$ to $1/(4\sigma_1^2)$. For realistic values of x and y the right-hand side of equation (A7) has only a small variation and can be assumed to be constant at first approximation

$$t - 3\epsilon u = K^2 ,$$

or:

$$1 + (1 - 3\epsilon)x^2 + (1 + 3\epsilon)y^2 = K^2 . \tag{A8}$$

The isodensity contours can be considered as ellipses with the same orientation as isopotentials but with ellipticities three times the isopotential ones.

In practice, we observed the isoluminosity contours and assume that they are the isomass-density contours. The ellipticity of the potential will be one-third the ellipticity given by the observables.

APPENDIX B

RELATIONS BETWEEN THE σ_{1D} AND σ_{los}

In the case of a circular potential, the analytical projected Newtonian potential used for the modeling reduces to

$$\Phi^{2D}(x) = \Phi_0^{2D}\sqrt{1 + x^2} , \tag{B1}$$

where $x = r/r_c$ and r_c is the core radius. The projected mass density is

$$\Sigma^{2D}(x) = \frac{\Phi_0^{2D}}{4\pi G r_c^2}\frac{2 + x^2}{(1 + x^2)^{3/2}} .$$

Furthermore, the three-dimensional mass density is given by Abel's integral of the deprojection:

$$\rho(y) = \frac{\Phi_0^{2D}}{4\pi G r_c^2}\frac{1}{\pi r_c}\frac{3 + y^2}{(1 + y^2)^2} ,$$

with $y = r'/r_c$ and r' is the three-dimensional radius. The unprojected potential is given by Poisson's equation, which finally gives

$$\Phi^{3D} = \frac{\Phi_0^{2D}}{2\pi r_c}\ln(1 + y^2) .$$

Let us write now Φ^{3D} and ρ as follows:

$$\Phi^{3D} = \Phi_0^{3D}\ln(1 + y^2) = \Phi_0^{3D}\chi = -\Psi ,$$

$$\rho = \rho_0\frac{3 + y^2}{(1 + y^2)^2} = \rho_0(2e^{-2\chi} + e^{-\chi}) .$$

For an isotropic velocity distribution, the variance of the velocity is 3 times the projected velocity dispersion, and the Jeans equation is

$$\frac{d\rho\sigma^2}{d\Psi} = \rho ,$$

which can be integrated

$$\rho\sigma^2 = \rho_0\Phi_0^{3D}(e^{-2\chi} + e^{-\chi}) .$$

Then,

$$\sigma^2(y) = \frac{2}{3}\Phi_0^{3D}\frac{1 + (y^2/2)}{1 + (y^2/3)} .$$

That is, the central velocity dispersion is related to the central three-dimensional potential by the following formula:

$$2\Phi_0^{3D} = 3\sigma_0^2 . \tag{B2}$$

Since the undimensioned projected potential is related to the central value of the three-dimensional potential,

$$\Phi_0 = \frac{2}{c^2}\frac{D_{LS}}{D_{OS}D_{OL}}\Phi_0^{2D} = \frac{2}{c^2}\frac{D_{LS}}{D_{OS}D_{OL}}2\pi D_{OL}r_c\Phi_0^{3D} ,$$

we can link the projected potential to the true velocity dispersion and the velocity dispersion as expressed in our analytical formula of the potential

$$\Phi_0 = 6\pi\left(\frac{\sigma_0}{c}\right)^2 \frac{D_{LS}}{D_{OS}} r_c = 4\pi\left(\frac{\sigma_{1D}}{c}\right)^2 \frac{D_{LS}}{D_{OS}} r_c \, .$$

The quantity σ_{1D} is the velocity dispersion used in our analytical formula. Therefore, the true three-dimensional central velocity dispersion is given by

$$\sigma_0^2 = \frac{2}{3}\sigma_{1D}^2 \, .$$

Finally, we can project the three-dimensional velocity dispersion to find σ_{los}, the line-of-sight velocity dispersion:

$$\sigma_{los}^2(y) = \frac{9}{8}\frac{1 + (2y^2/3)}{1 + (y^2/2)} \, .$$

This gives the true value of the central line-of-sight velocity dispersion compared to the velocity dispersion used to define the model:

$$\sigma_{los}^2(0) = \frac{9}{8}\sigma_0^2 = \frac{3}{4}\sigma_{1D}^2 \, .$$

The velocity dispersion must be reduced by a factor of $\sqrt{3}/2 \simeq 0.87$ to be comparable with numerical simulations.

APPENDIX C

χ^2 AND OBSERVATIONAL CONSTRAINTS FOR MODELING THE LENS

C1. WEAK DISTORTION REGIME

In the approximation of weak distortion, the source shape of the source is related to the image shape by

$$f^S = a^{-1} f^I (a^{-1})^T \, , \tag{C1}$$

where f^I and f^S are the two-dimensional deformation matrix and a^{-1} is the amplification matrix (Kochanek 1990):

$$a^{-1} = \begin{pmatrix} \kappa + \gamma\cos 2\varphi & \gamma \sin 2\varphi \\ \gamma \sin 2\varphi & \kappa + \gamma \sin 2\varphi \end{pmatrix} = \kappa I + \gamma R_\varphi S R_{-\varphi} = R_\varphi(\kappa I + \gamma S) R_{-\varphi} \, ,$$

where I is the identity matrix, S the shear matrix, and R_μ is the rotation matrix, which generate a rotation of μ. The quantity φ is the orientation of the major axis of the amplification matrix relative to fixed orientations. The convergence κ and the shear γ give the eigenvalues of the amplification matrix: $(\kappa + \gamma)$ and $(\kappa - \gamma)$.

The matrix f can be diagonalized and equation (1) gives

$$f^S = \lambda^S I + \Delta\lambda^S J_{\theta_S} = a^{-1}(\lambda^I I + \Delta\lambda^I J_{\theta_I}) a^{-1} \, , \tag{C2}$$

where $\lambda \pm \Delta\lambda$ are the eigenvalues of the deformation matrix, which can be expressed in terms of major and minor axes of the ellipses a and b: $\lambda = (a^2 + b^2)/8$, $\Delta\lambda = (a^2 - b^2)/8$, $\epsilon = \Delta\lambda/\lambda$. The quantity θ is the position angle of the major axis of the image (or source) relative to fixed orientations, and

$$J_\theta = R_\theta S R_{-\theta} = \begin{pmatrix} \cos 2\theta & \sin 2\theta \\ \sin 2\theta & -\cos 2\theta \end{pmatrix} .$$

By using the equation (1) and (2) we have

$$R_{-\varphi} f^S R_\varphi = \lambda^S I + \Delta\lambda^S J_{(\theta_S - \varphi)} = (\kappa I + \gamma S)(\lambda^I + \Delta\lambda^I J_{(\theta_I - \varphi)})(\kappa I + \gamma S) \, ,$$

or

$$\lambda^S I + \Delta\lambda^S J_{(\theta_S - \varphi)} = [(\kappa^2 + \gamma^2)\lambda^I + 2\kappa\gamma\Delta\lambda^I \cos 2(\theta_I - \varphi)] I + 2\lambda^I \kappa\gamma S + \Delta\lambda^i(\kappa^2 J_{(\theta_I - \varphi)} + \gamma^2 S J_{(\theta_I - \varphi)} S) \, . \tag{C3}$$

The trace and the components of each matrix relates the source to the image parameters:

$$\lambda^S = \lambda^I(\kappa^2 + \gamma^2)[1 - \epsilon_{pot}\epsilon_I \cos 2(\theta_I - \varphi)] \, , \tag{C4a}$$

$$\xi_S \cos 2(\theta_S - \varphi) = \xi_I \delta_{pot} \cos 2(\theta_I - \varphi) - \xi_{pot}\delta_I \, , \tag{C4b}$$

$$\xi_S \sin 2(\theta_S - \varphi) = \xi_I \sin 2(\theta_I - \varphi) \, , \tag{C4c}$$

where

$$\epsilon_I = \frac{a^2 - b^2}{a^2 + b^2}\,; \qquad \delta_I = \frac{a^2 + b^2}{2ab}\,; \qquad \xi_I = \frac{a^2 - b^2}{2ab}\,,$$

$$\epsilon_{\rm pot} = -\frac{2\kappa\gamma}{\kappa^2 + \gamma^2}\,; \quad \delta_{\rm pot} = \frac{\kappa^2 + \gamma^2}{\kappa^2 - \gamma^2}\,; \quad \xi_{\rm pot} = -\frac{2\kappa\gamma}{\kappa^2 - \gamma^2}\,.$$

The physical meaning of $\epsilon_{\rm pot}$ can be understood as follows. In the case $\xi_S = 0$ (circular source), the equations (C4*b*) and (C4*c*) give $\theta_I = \varphi$, and $\epsilon_I = \epsilon_{\rm pot}$. Then for circular sources, the ellipticities of weakly distorted images is simply given by $\epsilon_{\rm pot}$.

By using the triplet ($\xi_{\rm pot}$, $\epsilon_{\rm pot}$, $\delta_{\rm pot}$), the reversed equations which give λ^I as a function of λ^S have the same analytical shape and can be obtained directly from substituting the I and S indices of the image and the source and by changing the sign of $\epsilon_{\rm pot}$ and $\xi_{\rm pot}$.

The equations (C4*a*) to (C4*c*) are very easy to handle for the fitting. The minimization will be carried out by assuming a set of parameters for the potential, then by projecting each image in the source plane. Since we should have only one single source, the difference between each projected image should be minimum for the best-fitting model. The χ^2 writes

$$\chi^2 = \sum_{i=1}^{N} \frac{(w_{x_i} - w_{x_{i+1}})^2}{\sigma_{w_x}^2} + \sum_{i=1}^{N} \frac{(w_{y_i} - w_{y_{i+1}})^2}{\sigma_{w_y}^2} + \sum_{i=1}^{N} \frac{(\xi_{x_i} - \xi_{x_{i+1}})^2}{\sigma_{\xi_x}^2} + \sum_{i=1}^{N} \frac{(\xi_{y_i} - \xi_{y_{i+1}})^2}{\sigma_{\xi_y}^2}\,, \tag{C5}$$

with

$$\xi_x = \xi_S \cos 2\theta_S\,, \qquad \xi_y = \xi_S \sin 2\theta_S\,.$$

The summation is done on each projected image in the source plane, and the w's are the undimensioned center positions of images in the source plane given by the lens equation. For an analytical potential as written in Appendix A (eq. [A1]) the coordinates are

$$w_x = x^S \frac{r_c}{\Phi_0}\,, \qquad \text{and} \qquad w_y = y^S \frac{r_c}{\Phi_0}\,.$$

C2. CONSTRAINTS FROM HIGHLY MAGNIFIED IMAGES

In the high magnification regime, the shape parameters of merging images are not observables, and the relations between the source and the images as written above are not valid. Therefore, the giant arcs cannot give interesting constraints from the shape parameters of the merging images. However, we know that when the source moves close to the internal caustic, the major magnification axis φ is the direction formed by the two merging images. And this is obviously also the orientation of the major axis of the two elongated images θ_I. Therefore, at the crossing point where the external critical line crosses the tangent of the two merging images we have $\theta_I = \varphi$. This then adds three constraints: the crossing points ($x_{\rm cross}$, $y_{\rm cross}$) and $\theta_I = \varphi$.

APPENDIX D

POSITIONS OF THE CRITICAL LINES

In this Appendix, we show that the knowledge of the positions of both the radial and tangential arc from the observations gives immediately a rough estimate of the location of the internal and external critical lines and of the core radius as well. The demonstration is given in the case of small ellipticity for the potential, which is the case of interest for MS 2137−23.

Let us rewrite the projected potential in polar coordinates

$$\Phi(r, \theta) = \Phi_0 \sqrt{1 + \left(\frac{r}{r_c}\right)^2 (1 - \epsilon \cos 2\theta)}\,. \tag{D1}$$

The amplification matrix in polar coordinates is

$$\boldsymbol{M}^{-1} = \begin{pmatrix} 1 - \frac{1}{r}\frac{\partial\Phi}{\partial r} - \frac{1}{r^2}\frac{\partial^2\Phi}{\partial\theta^2} & -\frac{\partial}{\partial r}\left(\frac{1}{r}\frac{\partial\Phi}{\partial\theta}\right) \\ -\frac{\partial}{\partial r}\left(\frac{1}{r}\frac{\partial\Phi}{\partial\theta}\right) & 1 - \frac{\partial^2\Phi}{\partial r^2} \end{pmatrix}.$$

In the case of small ellipticity and small core radius we can neglect the term

$$\frac{\partial}{\partial r}\left(\frac{1}{r}\frac{\partial\Phi}{\partial\theta}\right).$$

Then the critical lines are given when one of the eigenvalues of the amplification matrix vanishes.

The tangential critical line is defined when the eigenvalue in the tangential direction is zero, hence by the equation

$$1 - \frac{1}{r}\frac{\partial\Phi}{\partial r} - \frac{1}{r^2}\frac{\partial^2\Phi}{\partial\theta^2} = 0\,.$$

The radial critical line is defined when the eigenvalue in the radial direction is zero, hence by the equation

$$1 - \frac{\partial^2 \Phi}{\partial r^2} = 0 .$$

In the peculiar case of a lens configuration which leads to a radial image of a source at redshift z_R and a tangential image of a source at redshift z_T, the critical lines can be expressed with the core radius r_c and the central three-dimensional velocity dispersion σ_0 of the potential (note that all radii are expressed in radians in the following formulae).

D1. TANGENTIAL ARC

For circular lenses $\epsilon = 0$, critical lines are circular, and the radius of the tangential arc is

$$r_T^2 = \left(6\pi \frac{\sigma_0^2}{c^2} \frac{D_{\rm LT}}{D_{\rm OT}} \right)^2 - r_c^2 ,$$

where the critical radius is expressed in radians. This equation shows that for a given tangential arc with known redshift, the velocity dispersion of the lens increases as the core radius increases. But, if we consider small ϵ, then we can neglect the terms in ϵ^2 and the critical line in the polar coordinates (ρ, θ) is

$$\rho_T^2 \left[1 - 3\epsilon \left(1 + \frac{2r_c^2}{3\rho_T^2} \right) \cos (2\theta) \right] = r_T^2 , \tag{D2}$$

which corresponds when $2r_c^2/3\rho_T^2 \ll 1$ to an ellipse with an ellipticity, 3 times bigger than the ellipticity of the potential (This only concerns the critical line. The ellipticity of the projected mass density is 3 times larger than the isopotentials).

D2. RADIAL ARC

In the same way the radial arc is given in the circular case by

$$r_R^2 = r_c^{(4/3)} \left(6\pi \frac{\sigma_0^2}{c^2} \frac{D_{\rm LR}}{D_{\rm OR}} \right)^{2/3} - r_c^2 .$$

This expression shows that radial arcs can only appear when the core radius is nonzero. And in the limit of small ϵ, the critical line in the polar coordinates is

$$\rho_R^2 \left[1 + \frac{\epsilon}{3} \left(\frac{2r_c^2}{\rho_R^2} - 1 \right) \cos (2\theta) \right] = r_R^2 , \tag{D3}$$

which corresponds to an ellipsoid of small ellipticity, compared to the potential.

Finally we can express the relation between the two critical radii r_T, r_R and the core radius r_c:

$$\left(\frac{r_R}{r_c} \right)^2 + 1 = \left(\frac{D_{\rm LR}}{D_{\rm OR}} \frac{D_{\rm OT}}{D_{\rm LT}} \right)^{2/3} \left[\left(\frac{r_T}{r_c} \right)^2 + 1 \right]^{2/3} . \tag{D4}$$

The observations give

$\rho_T = 15.5''$, $\theta_T = 56.^\circ 5 \pm 2^\circ$, where θ_T is the angle between the major axis of the potential and the vector radius from the center of the potential and the point where the external critical line crosses the tangential arc.

$\rho_R = 6''.2$, $\theta_R = 64^\circ \pm 0.^\circ 5$, where θ_R is equivalent to θ_T for the radial arc.

The equations (D2) and (D3) are only valid for small ellipticities, but in that case, since the left-hand side of equation (D2) must be positive, the core radius should be of the same order as the critical radius. Consequently, by using equations (D2) and (D3) we find that $r_T = 14''.8$ and $r_R = 6''.2$. And finally if we assume that the two sources are at a same redshift, then equation (D4) gives us the value of the core radius $r_c = 7''.4 \pm 0''.2$.

REFERENCES

Blandford, R. D., & Kochanek, C. S. 1987, ApJ, 321, 658
Briel, U. G., Henry, J. P., & Böhringer, H. 1992, A&A, 259, L31
Charlot, S., & Bruzual, G. A. 1991, ApJ, 367, 126
Dressler, A., & Gunn, J. E. 1982, ApJ, 263, 535
Eyles, C. J., Watt, M. P., Bertram, D., Church, M. J., Ponman, T. J., Skinner, G. K., & Willmore, A. P. 1991, ApJ, 376, 23
Fort, B., Le Fèvre, O., Hammer, F., & Cailloux, M. 1992, ApJ, 399, L125
Frenk, C. S., White, S. D. M., Efstathiou, G., & Davis, M. 1990, ApJ, 351, 10
Gerbal, D., Durret, F., Lima-Neto, G., & Lachièze-Rey, M. 1992, A&A, 253, 77
Gioia, I. M., Maccacaro, T., Schild, R. E., Wolter, A., Stocke, J. T., Morris, S. L., & Henry, J. P. 1990, ApJS, 72, 567
Grossman, S. A., & Narayan, R. 1988, ApJ, 324, L37
———. 1989, ApJ, 344, 637
Hammer, F. 1987, in Third IAP Astrophys. Meeting on High Redshift Galaxies', ed. P. Bergeron et al. (Gif-sur-Yvette: Editions Frontières), 467
———. 1991, ApJ, 383, 66
Hammer, F., & Rigaud, F. 1989, A&A, 226, 45
Kassiola, A., Kovner, I., & Blandford, R. D. 1992a, ApJ, 396, 10
Kassiola, A., Kovner, I., & Fort, B. 1992b, ApJ, 400, 41
Kneib, J.-P., Mellier, Y., & Longaretti, P.-Y. 1993, in Hamburg International Conference on Gravitational Lensing, ed. R. Kayser et al. (Berlin: Springer), in press
Kochanek, C. S. 1990, MNRAS, 247, 135
Kochanek, C. S., Blandford, R. D., Lawrence, C. R., & Narayan, R. 1989, MNRAS, 238, 43
Koo, D. C. 1987, in Large-Scale Motions in the Universe, ed. V. C. Rubin & G. V. Coyne (Princeton: Princeton Univ. Press), 523
Kovner, I. 1988, in The Post-Recombination Universe, ed. N. Kaiser & A. N. Lasenby (Dordrecht: Kluwer), 315
———. 1989, ApJ, 337, 621
Mellier, Y. 1993, in IV^e Rencontres de Blois, Particle Astrophysics, (Gif-sur-Yvette: Editions Frontières)

Mellier, Y., Soucail, G., Fort, B., Le Borgne, J.-F., & Pello, R. 1989, in Toulouse Workshop on Gravitational Lensing, ed. Y. Mellier, B. Fort, & G. Soucail (Berlin: Springer), 261
Mellier, Y., Soucail, G., Fort, B., & Mathez, G. 1988, A&A, 199, 13
Miralda-Escudé, J. 1991, ApJ, 370, 1
Narayan, R., & Grossman, S. 1988, in Gravitational Lenses, ed. J. M. Moran, J. N. Hewitt, & K. Y. Lo (Berlin: Springer), 31
Pelló, R., Le Borgne, J.-F., Soucail, G., Mellier, Y., & Sanahuja, B. 1991, ApJ, 366, 405
Petrosian, V., Bergmann, A. G., & Lynds, R. 1989, in Toulouse Workshop on Gravitational Lensing. Y. Mellier, B. Fort, & G. Soucail (Berlin: Springer), 254
Porter, A. C., Schneider, D. P., & Hoessel, J. G. 1991, AJ, 101, 1561
Smail, I., Ellis, R. S., Fitchett, M. J., Couch, W. J., Sharples, R. M., & Jørgensen, H. 1992, Durham preprint
Soucail, G., Fort, B., Mellier, Y., & Picat, J.-P. 1987, A&A, 172, L14
Stocke, J. T., Morris, S. L., Gioia, I. M., Maccacaro, T., Schild, R., & Wolter, A. 1991, ApJS, 76, 813
Tyson, J. A., Valdes, F., & Wenk, R. 1990, ApJ, 349, L1
van Kampen, E., & Rhee, G. F. N. R. 1990, A&A, 237, 283